CrossMark

A Dedicated DIC Methodology for Characterizing Plastic Deformation in Single Crystals

X. G. Wang[1,2] · J. F. Witz[2] · A. El Bartali[2] · A. Oudriss[3] · R. Seghir[2] · P. Dufrénoy[2] ·
X. Feaugas[3] · E. Charkaluk[2]

Abstract This paper focuses on the development of an appropriate Digital Image Correlation (DIC) methodology based on Image Registration and dedicated for characterizing the plastic deformation in single crystals. A pure nickel single crystal specimen is plastically deformed in tension and investigated by DIC technique. Based on the measured kinematic fields, the proposed method enables to identify the slip activity on the crystal surface and to locate precisely the slip band interfaces at microscale which behave as kinematic discontinuities. The computed displacement data are projected on a well-defined physical basis containing slip details, then the strain fields can be derived directly from a set of analytical functions. The possible errors in displacement induced by this projection approach are evaluated. Finally, some results of the evaluated strain fields are presented. It demonstrates that the developed DIC methodology allows quantitative characterization of a heterogeneous deformation process and promotes further relationships to be established between slip activity and strain field evolution in single crystals.

✉ E. Charkaluk
eric.charkaluk@ec-lille.fr

1 State Key Laboratory of Advanced Design and Manufacturing for Vehicle Body, College of Mechanical and Vehicle Engineering, Hunan University, 410082 Changsha, People's Republic of China

2 LML UMR CNRS 8107, Université Lille Nord de France, Bd. Paul Langevin, 59655 Villeneuve d'Ascq, France

3 LaSIE UMR CNRS 7356, Université de La Rochelle, Av. Michel Crépeau, 17042 La Rochelle, France

Introduction

Plastic deformation of crystals is a heterogeneous process. The deformation heterogeneity embodies at different time and space scales. At the microscopic scale, the discrete dislocations move along particular slip planes and interact with each other and with the obstacles, creating various structural configurations such as entanglements, junctions, walls and cells. These microstructural developments generally exhibit a strong tendency to cluster locally. It results in the formation of irregular deformation patterns, extending the heterogeneity to the mesoscopic scale and even to the macroscopic level [1].

With the recent progress on the multiscale modeling of crystal plasticity [2, 3], now there is an increasing need for corresponding "multiscale experiments" [1, 4]. As a matter of fact, the current approach for plasticity characterization operates mostly at two scales: one is at the microstructure scale based on evolution of dislocation structures [5–7] and the other is at the specimen scale on the basis of the macroscopic mechanical response [8–10]. The transition scales are, however, generally lacked in the relevant studies. The ideal experimental means for such a multiscale study should be able to characterize the plastic deformation across the spectrum of length scales, and to provide sufficient details on how various levels connect together. In particular, the characterization of deformation patterns at the mesoscale and macroscale is essential for making a bridge between the different scales.

The first attempts on quantifying the macroscopic deformation pattern can be dated to nearly a century ago. In the

SEM

pioneering work of Taylor and Elam [11] on crystal plasticity, they measured the orientation and shape change in aluminum single crystals through the scribed lines on the specimen surface. This philosophy was followed by applying refined methods for computing the deformation gradient matrix and by relating it with the slip activity [12, 13]. However, these methods can only give a global shape change in crystals but not a continuous strain field with sufficient local information.

Nowadays, the Digital Image Correlation (DIC) method [14–18] enables to provide full-field displacement and strain measurements, and have drawn the attention of many researchers. After a spectacular development in experimental solid mechanics, the DIC method has been used to characterize and quantify plasticity in polycrystals [19–22], oligocrystals [23, 24] and very recently single crystals [25, 26]. The application of the DIC method to the microstructure scale is an appealing research subject, and as well as a challenging one. The studies [1, 4, 22, 23, 27, 28] show that some reasonable mechanical discontinuities in crystal plasticity (e.g., grain boundaries, slip bands) can play an important role in the heterogeneous deformation process and bring about considerable manifestations in the kinematic field. In other words, the crystal surface can not be considered as continuum at the microstructure scale. And this effect can be much exaggerated when the grain attains to a millimeter size. Here it is worthy to note that it exists different versions of DIC method, namely the local approach [29] and the global approach [30]. Extensive examples [15, 17, 19, 30, 31] show that the image correlation strategy and algorithms adopted are closely associated with the specific case of deformation to be handled and as well as with the mechanical interpretation behind. Regarding a pertinent application of DIC method at the microstructure scale, some necessary considerations about the possible "discontinuities" (or structural information) should be embodied in the algorithm design, as the resulting displacement and strain fields are directly linked to the relevant mechanical interpretation. This is just the case of the present study.

The studied material in this work is a pure nickel single crystal specimen of millimeter size. The former study [32] on the same material has demonstrated the appearance of macroscopic slip bands on the specimen surface during plastic deformation. This paper aims to establish a new strategy in DIC computation, dedicated to the characterization of plastic deformation in single crystals which is possessed of a very heterogeneous nature.

This paper is organized as follows: in "Preliminaries - Image Registration" the theoretical framework of the applied DIC (or image registration) method is presented, in which the data treatment strategy specialized for single crystal deformation is outlined. In "Material and Experimental Procedure" the testing material is described and the experimental procedure is summarized. "Methodology Development" details the complete development of the data treatment procedure of the proposed DIC methodology adapted to single crystals. Some results of the calculated strain fields are presented and discussed in "Results of Strain Field Evolution". Finally, some concluding remarks are given in "Conclusion".

Preliminaries - Image Registration

In this work, "elastix" [33, 34], an open-source software initially designed for medical image registration, is adapted for DIC application, i.e., the assessment of displacement and strain fields. There is actually no genuine difference between these two terms: DIC and image registration. The former is usually specific to the field of solid mechanics, and the later represents a more general concept widely employed in the fields of computer vision [35], medical imaging [36], etc. In the present section the employed framework of image registration method will be briefly outlined, partly as a means to introduce the chosen notation.

Two images are involved in the image registration, which characterize the original and deformed surface of a material subjected to a known loading. An image is a scalar function of the spatial coordinate and of time that gives the gray level at each discrete point (or pixel) of coordinate x. The images of the reference and deformed states are called $f(x)$ and $g(x)$, respectively. The displacement field $u(x)$ of each material point is necessary to be introduced. Thus, this field allows one to relate the two images by requiring the conservation of the optical flow [37] on the material surface during the test

$$f(x) = g[x + u(x)] = g[T(x)] \qquad (1)$$

where $T(x) = x + u(x)$ is defined as the transformation, and $g[T(x)]$ is generally called as the corrected deformed image.

The goal of the image registration is to solve the problem of finding a transformation $T(x)$ that makes $g[x+u(x)]$ spatially aligned to $f(x)$. The quality of alignment is defined by a distance or similarity measure S. Because this problem is ill-posed for nonrigid transformations T, a regularization or penalty term P is often introduced that constrains T.

Commonly, the registration problem is formulated as an optimization problem in which the cost function C is minimized with respect to T

$$\hat{T} = arg\ minC[T; f(x), g(x)] \qquad (2)$$

$$C[T; f(x), g(x)] = -S[T; f(x), g(x)] + \gamma P(T) \qquad (3)$$

where γ weights similarity against regularity.

Several metrics (or correlation coefficients) are available for the similarity measure [33]. The NCC (Normalized Cross-Correlation) criterion is employed in this work with the following definition

$$S = \frac{\sum_{x_i \in \Omega_F} (f(x_i) - \bar{f})(g[T_\mu(x_i)] - \bar{g})}{\sqrt{\sum_{x_i \in \Omega_F} (f(x_i) - \bar{f})^2 \sum_{x_i \in \Omega_F} (g[T_\mu(x_i)] - \bar{g})^2}} \quad (4)$$

with Ω_F the domain of the fixed image $f(x)$, and the average gray values $\bar{f} = \frac{1}{|\Omega_F|} \sum_{x_i \in \Omega_F} f(x_i)$ and $\bar{g} = \frac{1}{|\Omega_F|} \sum_{x_i \in \Omega_F} g[T_\mu(x_i)]$ where $|\Omega_F|$ represents the number of pixels.

In the case that the penalty term P is absent, the cost function C equals to the minus S. In order to minimize the cost function or say to maximize the similarity function in (4), the parametric method is generally adopted. In parametric methods, the number of possible transformations is limited by introducing a parametrization model of the transformation. The original optimization problem thus becomes

$$\hat{T}_\mu = arg\ min C[T_\mu; f(x), g(x)] \quad (5)$$

where the subscript μ indicates that the transform has been parameterized.

The transformation T_μ or called shape function [15] is a key element in the image registration, which may have major influence on the calculated displacement and strain fields. The transformation model used for T_μ determines what type of deformations between the reference image and deformed image is attended. Concerning the case of a heterogeneous deformation process, the B-spline transformation is preferentially to be employed thanks to its excellent capacity on describing a free-form deformation [29, 33, 38, 39]. In elastix the B-splines are used as a parameterization

$$T_\mu(x) = x + \sum_{x_k \in N_x} p_k \beta^3 \left(\frac{x - x_k}{e} \right) \quad (6)$$

with x_k the control points, $\beta^3(x)$ the cubic multidimensional B-spline polynomial [39], p_k the B-spline coefficient vectors, e the B-spline control point spacing, and N_x the set of all control points within the compact support of the B-spline at x.

The control points x_k are defined on a regular grid overlaid on the reference image. The parameter e presents the grid spacing or grid size. A large e allows modeling of global nonrigid deformations, while a small e allows modeling of highly local nonrigid deformations [38]. A sensible choice of the value e is often crucial for a correct estimation of displacement fields. It could be particularly important for the case of single crystal deformation in which the strain has a strong tendency to localize, generating therefore special deformation patterns on the crystal surface.

Besides, in order to reduce both the data and transformation complexity, a multi-resolution approach [33] is generally recommended. The principle is to first treat the data under lower resolutions based on coarse grids made of a relatively large number of pixels. It allows providing the first estimates with less satisfactory precision. Then the DIC calculations are performed under higher resolutions with finer grids made of reducing number of pixels. And the estimation precision of the DIC is improved accordingly. The final resolution could eventually go down to one pixel as the grid size. This multi-resolution approach is also named by the multi-scale approach.

A complete development of the proposed DIC methodology dedicated to single crystals will be detailed after the presentation about the material and experimental procedure in the next section. It is worth noting that the observed surface feature of the deformed single crystal provides valuable information guiding for the development of this new strategy in DIC.

Material and Experimental Procedure

Nickel single crystals of very high purity (99.999 %) were obtained using the Bridgman technique along the crystal direction [001]. The material was initially supplied in the form of cylindrical rod and was further machined into dog-bone shaped specimens [32]. The geometric dimensions of the final obtained specimen are illustrated in Fig. 1.

Figure 1 shows also the orientation of the specimen: the observation surface is in the crystallographic plane (100) and the axial loading direction is along [001]. As the crystal structure of nickel is the face-centered cubic (fcc), it has therefore 12 possible slip systems of type {111}⟨110⟩. From a pure geometrical point of view, 8 slip systems will be equally loaded in the tensile test with the same Schmid factor equal to 0.4, and among them 4 active slip systems will intersect with the (100) plane, resulting in thus two groups of traces (slip bands) on the specimen surface. They are
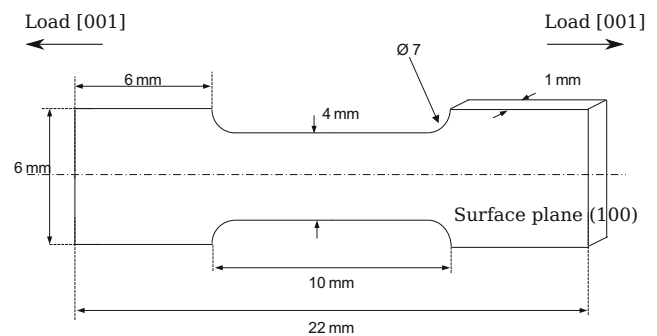
Fig. 1 The geometry of the nickel single crystal specimen

actually the intersections of the slip planes from two pairs of slip systems: $[101](11\bar{1})$-$[10\bar{1}](1\bar{1}1)$ and $[10\bar{1}](111)$-$[101](1\bar{1}\bar{1})$, as schematically presented in Fig. 2. Both of the two groups of slip bands are along the 45° slip direction with respect to the axial direction, and their intersection angle is also 45°. The above prediction was verified in former experiments [32] on the same material, which showed that the appearance of two groups of slip bands can be found on the specimen surface after plastic deformation.

For the purpose of DIC measurement, the specimen surface was sprayed by speckled paint using airbrush. The tensile test was performed using a micro tensile test stage of Kammrath & Weiss with a maximum force up to 5 kN. The test was controlled in displacement mode at a constant speed 19 $\mu m/s$, equivalent to a strain rate about 2×10^{-3} s^{-1}, and the imposed total strain was about 22 %.

In-situ DIC imaging system was used to investigate the deformation evolution during tensile test. Images of the specimen surface were captured using an Elphel CMOS camera made of 2592×1936 pixels. A Tamron 23FM50SP 50 mm lens was equipped that allowed a final spatial resolution of 10.8 $\mu m \times 10.8$ μm per pixel and a field of view of 10.4 $mm \times 7.9$ mm. In the tensile test, the specimen was loaded in a continuous mode without pause, and simultaneous image acquisition was conducted at a frequency of 15 HZ. Thus the whole deformation history of the specimen surface was recorded. The experimental set-up is shown in Fig. 3. More details of the micro tensile test stage is shown in Fig. 4.

It is suggested to observe the deformation pattern appearing on the specimen surface first before proceeding the kinematic field analysis. Figure 5 illustrates the deformed specimen after removing the surface coating by using acetone.

Figure 5 shows two groups of slip markings appearing on the specimen surface, as predicted by the former geometric analysis. One group of slip markings, however, is
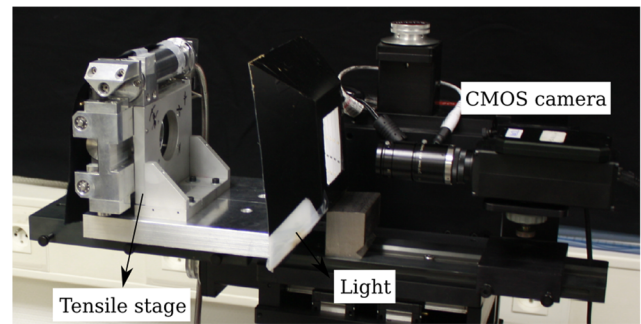

**Fig. 3** The experimental set-up of the test and measurement system

much more pronounced than the other. It means that an ideal "equally loaded" condition actually does not exist in a real crystal deformation, so the activations of the 8 slip systems with an equal Schmid factor of 0.4 can not simultaneously occur in a tensile test. This conclusion is in agreement with the study of Hauser and Jackson [40]. Hence, it is reasonable that some slip systems tend to be activated earlier and be deformed more than the others. For the sake of convenience, the more pronounced slip band is called as the primary slip band and the other the secondary slip band.

The strain localization is demonstrated clearly in the deformed specimen surface, and the band-shaped deformation patterns are directly linked to the slip activation. These are instructive information for quantifying the deformation field through an appropriate strategy in DIC that is presented in the following section.

Methodology Development

The developed methodology can be broken down into four parts: 1) Transformation Model, 2) Projection Basis, 3) Approximation Approach and Validation and 4) Strain Field Assessment.

Fig. 2 Four active slip systems with two pairs of intersections (group 1 and group 2) on the specimen surface

A3 - $[101](1\bar{1}\bar{1})$
B4 - $[10\bar{1}](111)$
C3 - $[101](11\bar{1})$
D4 - $[10\bar{1}](1\bar{1}1)$
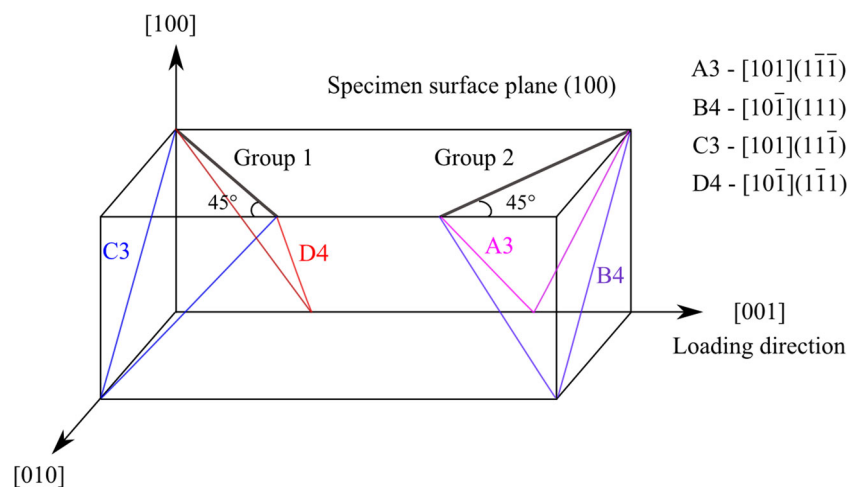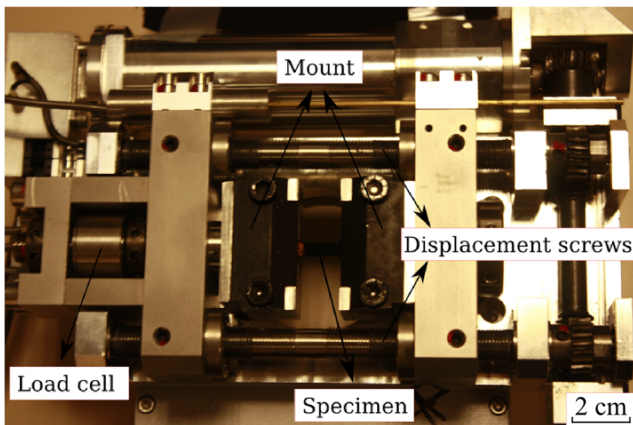
Fig. 4 The micro tensile test stage

Transformation Model

As mentioned in "Preliminaries - Image Registration", the grid spacing e (or grid size) governs how fine the structure is expected to be modeled. With smaller e, a smaller and more local deformation can be described. Thus the parameter e is generally desired to be as small as possible. But when it is small enough, it may cause the DIC computation to be very sensitive to noise. Then a tradeoff must be found between the characterization capacity on local strain and signal-to-noise ratio. The determination of a suitable grid spacing depends on several factors, e.g., the strain localization level, speckled paint quality, and image resolution. Normally the strain localization level is considered as the dominant factor. Specific to the current study on single crystal deformation, it may refer to the width of the slip band. One can conceive that if the chosen grid spacing is higher than the band width, it is thus not assured that the local strain within the band could be properly characterized. Figure 5 reveals that the average width of the apparent slip bands of the deformed specimen is about 200 μm, or 19 pixels under the adopted optical resolution of DIC system. Hence, it is recommended to choose the grid spacing around 19 pixels, but the value
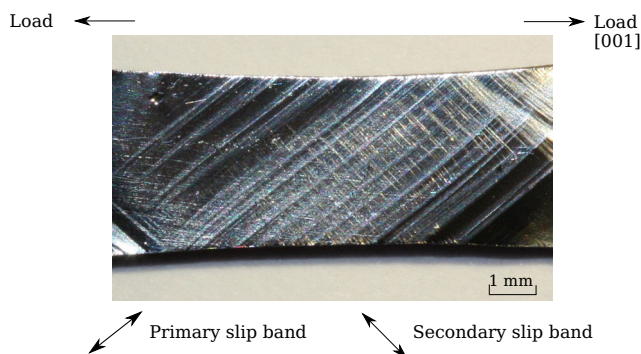
Fig. 5 The appearance of slip bands on the deformed specimen surface

could be fluctuated in a relatively large range since the adopted selection strategy is essentially semiempirical.

B-spline transformations with different grid spacing were tested in this work, and the selected e values included 64 pixels, 16 pixels and 4 pixels. An analysis by comparing their resulting displacement fields, especially the first two, was carried out. Figure 6(a) and (b) show the axial displacement fields for the final deformation state obtained by choosing the grid spacing $e = 64$ pixels and $e = 16$ pixels, respectively.

The axial displacement field in Fig. 6(a) manifests a rather global and smoothed spatial feature, where no local discontinuity associated with slip activation is noticeable. This result should be attributed to the oversized grids ($e = 64$ pixels), thus a "too" global scheme. On the contrary, the axial displacement field shown in Fig. 6(b) allows capturing the band-shaped heterogeneities due to the slip manifestations on the material surface. This is the outcome of a smaller grid size adopted ($e = 16$ pixels).

Similar results can be found in the transverse displacement fields, as shown in Fig. 7 concerning the final deformation state that corresponds to Fig. 6. The displacement field in Fig. 7(b) obtained using $e = 16$ pixels shows even more distinctive bands than those in Fig. 6(b), and the displacement field in Fig. 7(a) obtained using $e = 64$ pixels demonstrates a global pattern constantly.

Here it is worthy to note that only one group of slip bands is noticeable in the displacement fields, but not two. It is actually in agreement with the surface observation shown in Fig. 5. As one group of slip bands is much more pronounced than the other in the morphology, it is reasonable that it also dominates in the kinematic field. Hence, the appearing bands in Fig. 6(b) and (b) are reasonably corresponding to the primary slip bands.

A finer grid spacing $e = 4$ pixels was also tested in this analysis. The resulting displacement fields, however, are found rather noisy, as shown in Fig. 8 for both the axial and transverse displacement fields. Both Fig. 8(a) and (b) exhibit that the displacements along the slip direction are much less well-shaped comparing to the previous results using $e = 16$ pixels. In this case, the grid size must be increased so as to capture sufficient kinematic signals and to better distinguish the bands associated with slip activation.

It is necessary to point out that our DIC strategy is to choose the parameters that allow characterizing the local kinematic behavior of slip bands during deformation. The grid spacing is considered as a key parameter in this strategy. It has already shown that the calculated displacements can be substantially different with altered choices: a oversized grid ($e = 64$ pixels) can smooth out the essential local displacements and a too small grid ($e = 4$ pixels) may introduce unnecessary noises in the computation. When the grid spacing e equals to 16 pixels, it can avoid both of the two unfavorable situations, approaching therefore to an optimal

Fig. 6 The axial displacement fields (in pixel) for the final deformation state obtained using grid spacing (**a**) $e = 64$ pixels and (**b**) $e = 16$ pixels

(a)

(b)
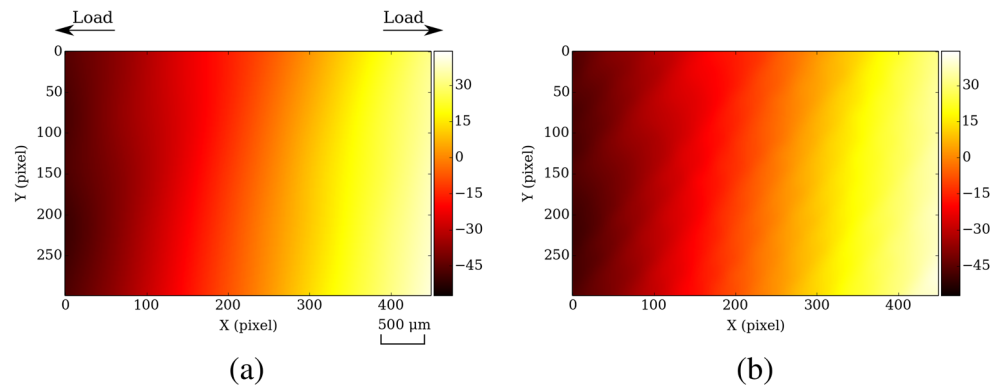
effect. On the one hand it enables to preserve the essential mechanical signals related to slip activation, and on the other hand it avoids the introduction of unexpected noises.

According to the above analysis, the grid spacing is determined as 16 pixels in the B-spline transformation. Besides, other key parameters involved in DIC computations are also determined. It mainly includes: the selection of NCC as the metric, the application of a 3rd order B-spline for sub-pixel interpolation and the use of a multi-resolution approach with four decreasing calculation steps (8 pixels, 4 pixels, 2 pixels and 1 pixel).

The acquired images during the tensile test are processed using the adopted DIC algorithm, which provides the initial displacement fields (axial and transverse). Here we call them "initial" displacement fields, as they will be further treated by a projection method proposed in this work. Indeed, the evaluated displacement fields are, in their initial form, not applicable for the derivation of strain fields, because they are possessed of strong and ill-defined discontinuities associated with slip activation. Without a proper consideration of the discontinuity nature of the displacement field, it may introduce important errors in the calculation of strain by differentiation. The philosophy of the projection method is to first establish a projection basis made of bands, which defines explicitly the boundaries of the individual continuous zones corresponding to the slip bands. And then the initial displacements are approximated

locally in each band through analytical functions, thus the strains in each band can be derived analytically.

Projection Basis

The measured displacement field shows the existence of the band-shaped heterogeneities associated with slip activity, which needs to be quantified. These bands are actually the kinematic manifestations of the slip bands on the material surface during plastic deformation. The interface between a slip band and an interslip band is considered as a "displacement discontinuity", which corresponds to a displacement jump when a local slip activation takes place. The idea of "projection" is to take into account the displacement discontinuity and to treat the data within a band where the displacement is considered continuous (under the current measurement scale), and then band by band for the whole displacement field.

The first step for realizing such a projection scheme is to locate the slip interfaces (or discontinuities) precisely in the displacement fields, thus determining a projection basis. In this analysis, the projection basis is defined pertaining to the final deformation state, in which all the bands are present on the material surface. Because the manifestations of the secondary slip bands appear too weak in the measured kinematic field, so only the primary slip bands are taken into account in this treatment.

Fig. 7 The transverse displacement fields (in pixel) for the final deformation state obtained using grid spacing (**a**) $e = 64$ pixels and (**b**) $e = 16$ pixels

(a)

(b)
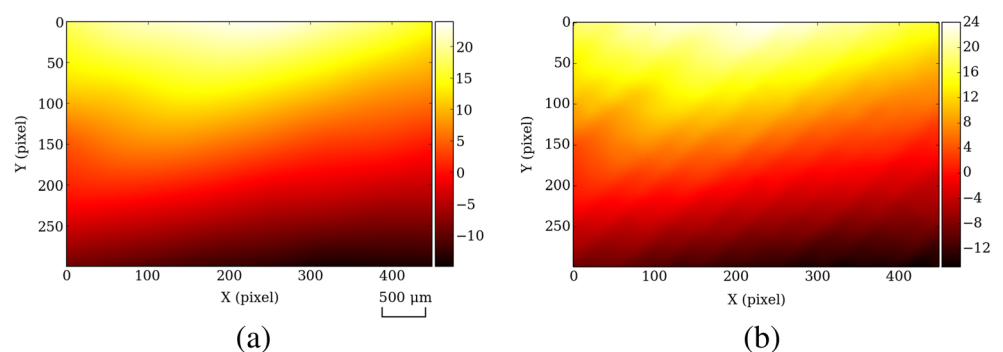
Fig. 8 The displacement fields obtained using grid spacing $e = 4$ pixels: (**a**) axial displacement and (**b**) transverse displacement

(a)

(b)
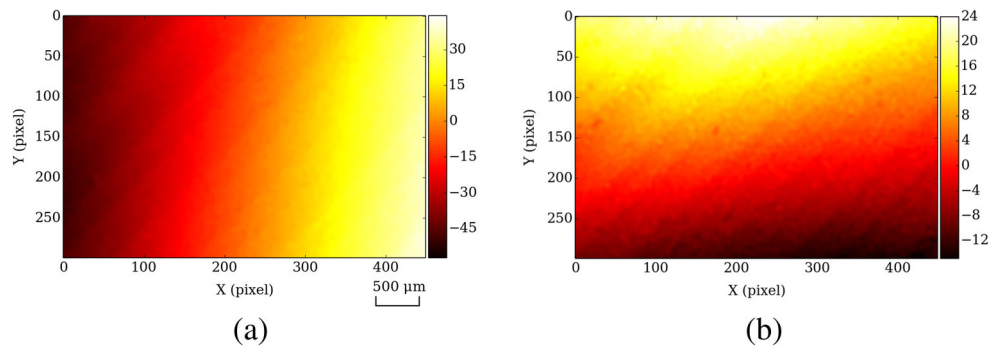
In order to better capture the local glide behavior of slip bands in the displacement fields, the "homogeneous" component of the displacement field due to the global elongation of specimen are preferred to be removed. As presented in the last section, the displacement field obtained using a grid spacing 64 pixels represents a rather global distribution without the presence of local glide movements. Its average displacement is actually very close to the one obtained using a grid spacing 16 pixels, with a slight difference about 0.4 %. Hence, to remove this homogeneous displacement component provides a possibility to access the displacements purely related to the local slip behavior. As a simple solution, it can be achieved by

$$U_{res} = U_{e16} - U_{e64} \qquad (7)$$

where U_{e16} represents the displacement field obtained using $e = 16$ pixels and U_{e64} the displacement field using $e = 64$ pixels.

The residual displacement U_{res} is considered pertaining to the local slip behavior of the material. Its corresponding axial and transverse displacement fields are shown in Fig. 9(a) and (b), respectively.

Figure 9 shows that a very similar pattern can be found in the resolved axial and transverse displacement fields, where the appearing bands are in the same positions (but in opposite colors). Two kinds of bands can be noticed: the ones with positive values in light color and the others with negative values in dark color. They appear in an alternate

mode, which represents well the slip behaviors of the adjacent bands (slip band and interslip band) that move in the opposite directions. Hence, the sought "interfaces" can be defined as the boundaries between the "light" bands and the "dark" bands.

For a precise location of the slip interfaces, the displacement values in the residual displacement fields of Fig. 9 were averaged along the predetermined slip direction (45° with respect to the axial direction), as marked in Fig. 9(b). The resulting average displacements for both axial and transverse displacement fields are illustrated in Fig. 10. The horizontal axis in the figure represents the normal direction with respect to the slip.

Figure 10 shows that the averaging axial and transverse displacements along the slip direction are almost symmetric to the axis of zero displacement. In this analysis, an assumption for the interface detection is made: the middle point between the "peak" and "valley" of a wave shown in Fig. 10 is considered as an interface point. It stands for the centre of transition connecting two zones with opposite slip movements. This method was applied respectively to the axial and transverse displacements, which led to quite the same results. The detected interface points for the axial displacement are illustrated in Fig. 11. It can be found that for most of the interface points (except two points), they are located right on or very close to the zero displacement axis. It is quite a logical result as the displacement of an interface between two bands with opposite signs (in displacement) is reasonably approaching to zero.

Fig. 9 The residual displacement U_{res}: (**a**) axial displacement field and (**b**) transverse displacement field


(a)

(b)
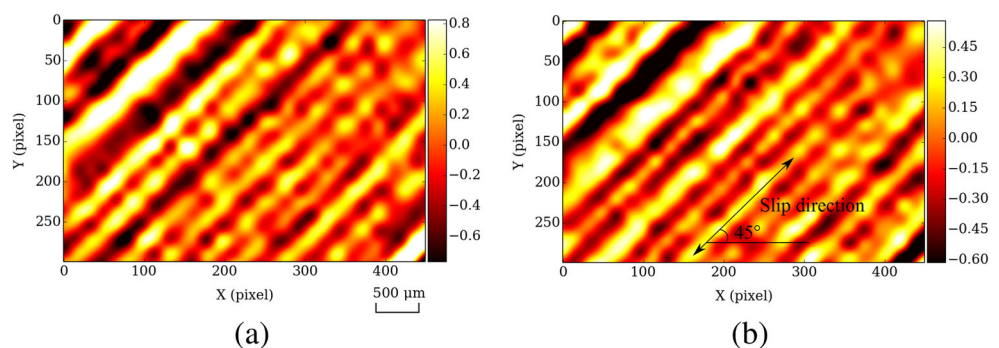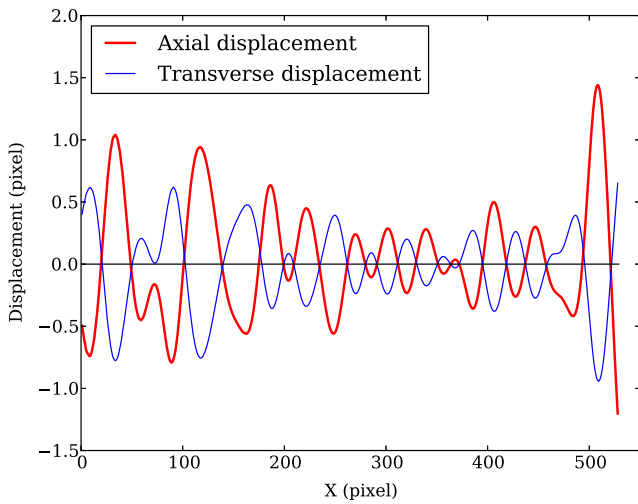
Fig. 10 Axial and transverse displacements averaged along the slip direction
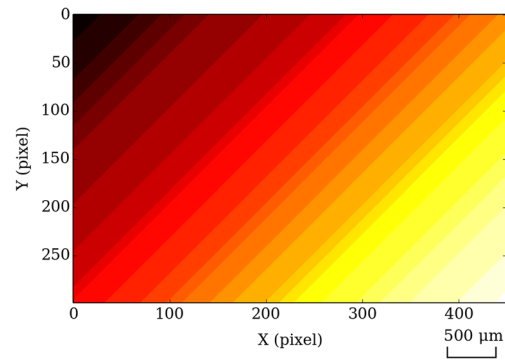
The interfaces determined in Fig. 11 can be projected to a 2D field by assuming that the slip bands are straight and along exactly the 45° slip direction according to the geometric prediction of single crystal deformation. Under this hypothesis, the projection basis can be built up through image segmentation according to the detected slip bands or interslip bands, and the result is shown in Fig. 12. There are 24 interfaces in total, thus 25 segmentation zones (or bands) constitute as the projection basis. Here the use of the varying colors serves only for the differentiation of the different bands.

Approximation Approach and Validation

The projection basis represents the heterogeneous deformation pattern appearing on single crystal surface: the active
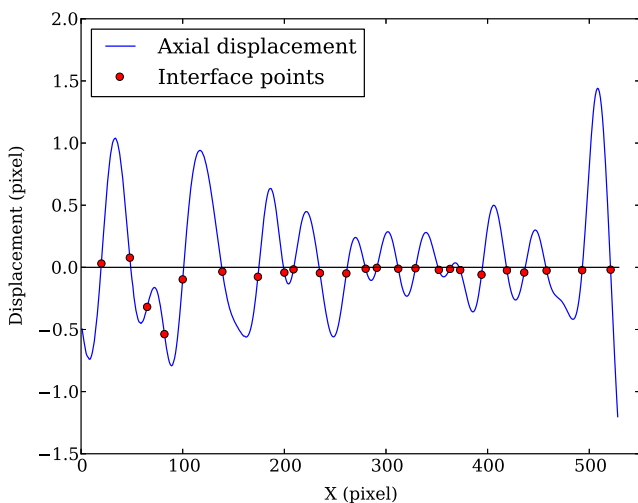
Fig. 11 The detected interface points

slip bands demonstrate a different deformation mechanism than the interslip bands, and the interface between each pair of them acts actually as a kinematic discontinuity. If this discontinuity is not taken into account in the strain calculation from displacement fields, using a general differential approach, e.g., finite difference method, may produce important errors due to the displacement jumps at the slip interfaces.

Concerning the projection method, the displacement data in each band of projection basis are expected to be fitted into an analytical function, then the strain in each band can be differentiated analytically. In this way, the strains are evaluated by taking into consideration of the deformation discontinuities appearing on single crystal surface. In this analysis, a second-order polynomial was adopted as the form of the analytical function of projection.

The displacements in each band can be fitted into two second-order polynomial functions F_{u_x} in the axial direction and F_{u_y} in the transverse direction

$$F_{u_x} = a_0 + a_1 x + a_2 y + a_3 x^2 + a_4 y^2 + a_5 xy \qquad (8)$$

$$F_{u_y} = b_0 + b_1 x + b_2 y + b_3 x^2 + b_4 y^2 + b_5 xy \qquad (9)$$

where a_k ($k = 0, 1, ...5$) is a set of constants associated with the axial displacement u_x and b_k ($k = 0, 1, ...5$) that with the transverse displacement u_y, and x and y are the two variables in the Cartesian coordinate system.

The above equations show that the displacements after the second-order polynomial fitting are parabolic within each band, thus the solved strain components are bilinear within each band. Nevertheless, before the strain calculation it is important to evaluate the possible errors in displacement due to the projection treatment.

The initial displacement result provided by the B-spline transformation without projection is considered as the reference for the error evaluation. Now concerning the final deformation state, Fig. 13 shows the comparison of the axial displacements before and after projection for a selected


Fig. 12 The projection basis
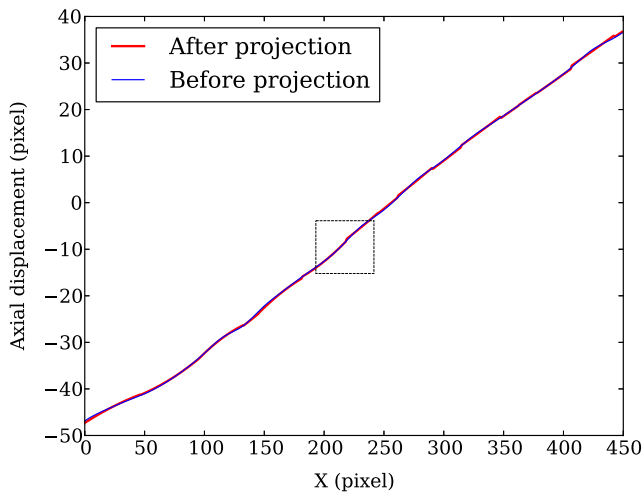
Fig. 13 The comparisons of the displacements before and after projection in axial displacement

line along the horizontal direction and in the middle of the image.

Figure 13 shows that the displacement curves before and after projection are basically overlapped, in which it is difficult to distinguish one from the other. In this case, a local zoom on the illustrated curve is applied. The selected zone for zooming is marked in Fig. 13, and the comparison after zooming is illustrated in Fig. 14.

In Fig. 14 the displacement after projection demonstrates very slight difference to the one without projection. Nevertheless, some relatively important local variation can still be noticed in the projected displacement curve, which shows a local shift to the initial displacement curve. This kind of local shift (or discontinuity) is generally corresponding to the location of the slip interface, which is a reasonable result by applying the band-based projection approach. The
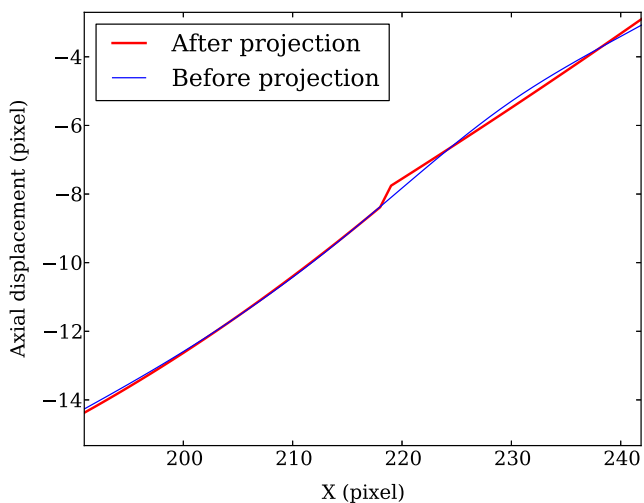
Fig. 14 A zoom on the zone marked in Fig. 13

same observation can be verified in the transverse displacement field, which will not be detailed here.

The above analysis shows that the projection treatment does not introduce additional errors in displacement. It, therefore, validates the applied approximation approach at least from a metrological viewpoint. The axial and transverse displacement fields after projection are illustrated in Fig. 15(a) and (b), respectively. They show that the slip interfaces can be more easily distinguished in the projected displacement fields.

Strain Field Assessment

Based on the second-order polynomial functions in (8) and (9), the three in-plane strain components, axial strain (ε_{xx}), transverse strain (ε_{yy}) and shear strain (ε_{xy}), can be obtained through

$$\varepsilon_{xx} = \frac{\partial F_{u_x}}{\partial x} = a_1 + a_5 y + 2a_3 x \tag{10}$$

$$\varepsilon_{yy} = \frac{\partial F_{u_y}}{\partial y} = b_2 + b_5 x + 2b_4 y \tag{11}$$

$$\varepsilon_{xy} = \frac{1}{2}\left(\frac{\partial F_{u_x}}{\partial y} + \frac{\partial F_{u_y}}{\partial x}\right) = \frac{1}{2}[a_2 + b_1 + (a_5 + 2b_3)x + (b_5 + 2a_4)y] \tag{12}$$

Since the parabolic interpolation is adopted, it leads to a bilinear distribution of strain in each band, as shown by the above equations.

In this study, an equivalent von Mises strain ε_{eq} is adopted in order to characterize the deformation in each slip plane. Here, the ε_{eq} is defined from the three obtained in-plane strain components (ε_{xx}, ε_{yy}, ε_{xy}) through

$$\varepsilon_{eq} = \sqrt{\frac{2\left(\varepsilon_{xx}^2 + \varepsilon_{yy}^2\right)}{3} + \frac{4\varepsilon_{xy}^2}{3}} \tag{13}$$

The three in-plane strain components for each acquired image were calculated by the proposed projection method, resulting in a corresponding equivalent von Mises strain ε_{eq} in each band for each moment. In this way the evolution of the equivalent von Mises strain during the tensile test can be obtained in each band.

Here it is also interesting to compare the strain fields obtained by using the proposed method with the ones obtained by an ordinary DIC procedure, in order to see how much improvement could be achieved. Such comparisons were conducted at different deformation stages, and a representative example is shown in Fig. 16. The image

Fig. 15 The displacements after the projection: (**a**) axial displacement field and (**b**) transverse displacement field

(a)

(b)
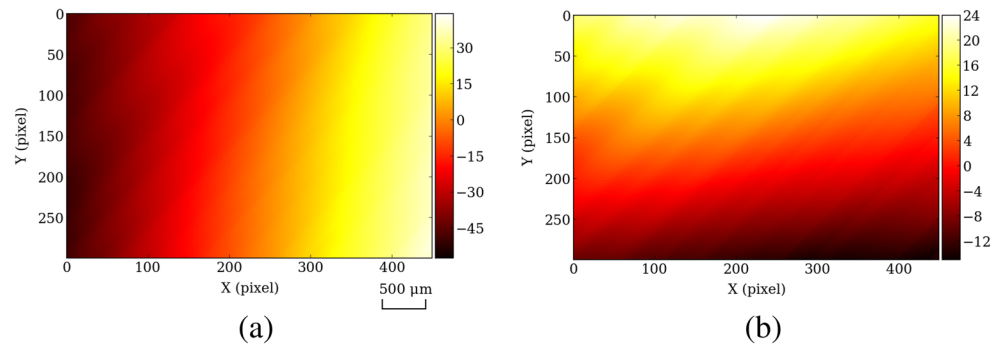
(a) presents the axial strain field obtained using an ordinary DIC procedure adopting the B-spline transformation with $e = 16$ pixels, in which the strain is derived from displacement by finite difference. The image (b) presents the axial strain field obtained by the projection method on the basis of the same data. Both strain fields show a single slip band activated. But one can remark that the slip band is better shaped after processing by the projection method, and the noises in other regions impertinent to slip activation have been also well smoothed. The example demonstrates that the projection method enables to deliver more explicit and useful information that may facilitate the interpretation of the microstructure-related strain evolution. It could be particularly helpful in the case that when the noise level is elevated comparing to the local strain.

Some preliminary results regarding the strain field evolution of nickel single crystal specimen are presented in the next section.

Results of Strain Field Evolution

Figure 17 illustrates the macroscopic axial stress-strain curve of specimen during the tensile test. A series of calculated equivalent von Mises strain fields labeled A-E is also displayed in Fig. 17.

At early stages of deformation, as shown by strain field A, no particular strain localization associated with slip activation is noticed. The following stages of deformation present, however, a strong heterogeneous strain distribution. As observed in strain fields B and C, the strains are well-shaped and localized within certain domains which exhibit much higher deformation levels than the other areas. At final stages of deformation, shown by strain fields D and E, the strain heterogeneity pattern tends to be stabilized, without showing notable changes with increasing deformation. Here it is worth noting that since the projection basis is built depending on the final deformation state, some band boundaries in the strain field could be artificial ones before actual slip activation. The artificial band boundaries can normally be well recognized as they are mainly in the early deformation stages appearing rather weak and discontinuous.

The above observation is believed to have a direct link with the slip activation, more specifically, the emergence and development of slip bands on the specimen surface. For a further quantitative investigation, a so-called band-based analysis was employed. In this method, the average strain in each band is used to represent the deformation level of the band. By this means, both spatial and temporal evolution of strain fields can be analyzed in a simplified manner by taking the band as the basic analysis element.

(a)

(b)
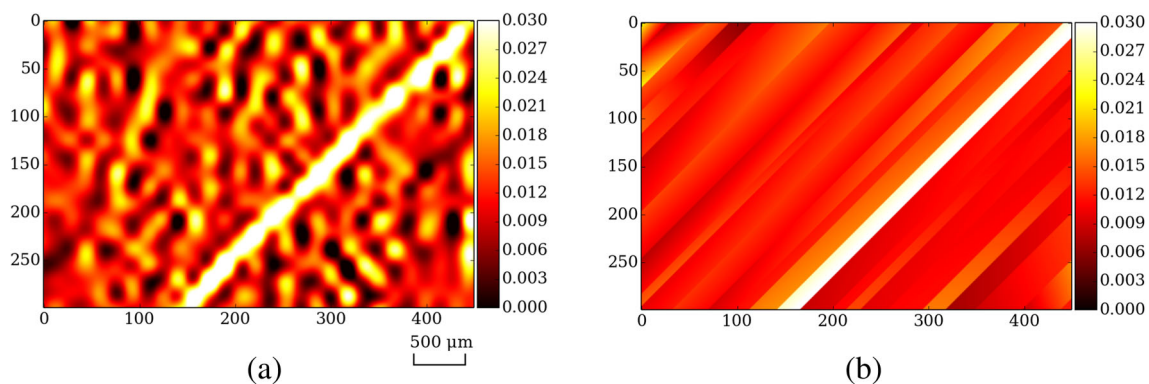
Fig. 16 The axial strain fields obtained by using: (**a**) an ordinary DIC procedure and (**b**) the proposed projection method

Fig. 17 The macroscopic axial stress-strain curve of specimen and the calculated equivalent von Mises strain fields for corresponding points along the curve
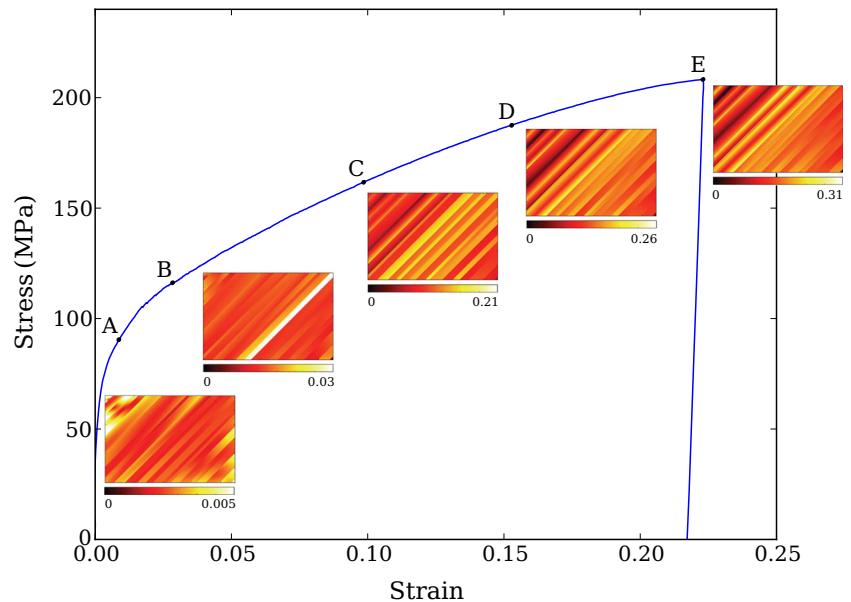

Figure 18 exhibits the evolution trend of ε_{eq} in the early deformation stage, in which three strain curves at different macroscopic strain levels (0.6 %, 1.2 %, 1.8 %) are illustrated. In the figure, each band is denoted by a reference number i in the abscissa axis. The curves in Fig. 18 demonstrate that a general low strain level is found in this stage and the strain in one band does not exhibit a significant difference from that of others. With the increasing load in the tensile test, the average strain level increases but the strain distribution pattern remains relatively stable. Thus, from the viewpoint of strain heterogeneity, the early deformation stage is governed by a quite homogeneous deformation regime from band to band.
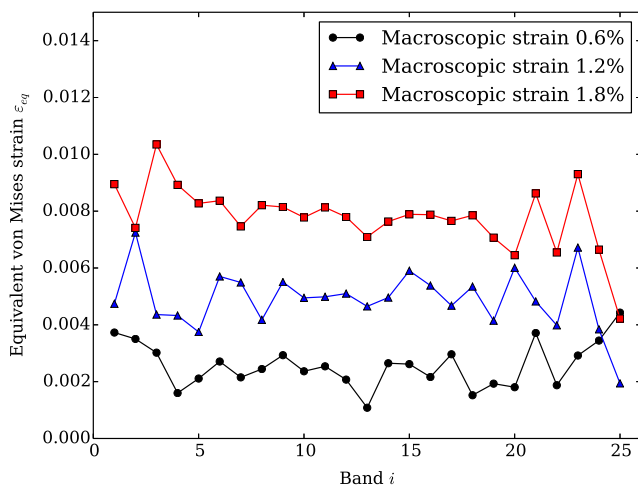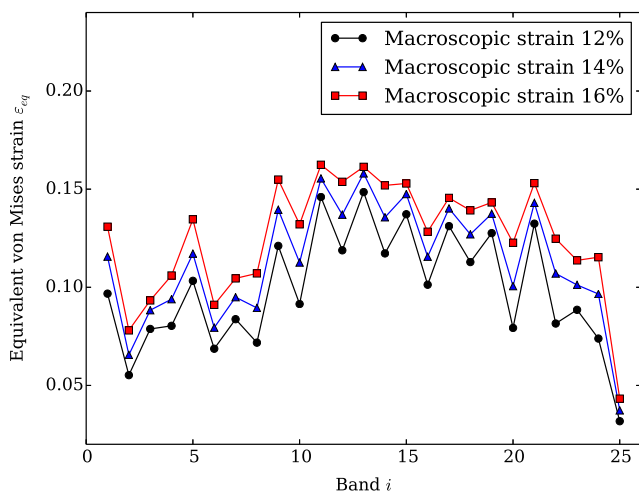
The strain evolution trend in the subsequent deformation stage can be illustrated in Fig. 19 where three strain curves at different macroscopic strain levels (2.2 %, 3 %, 6 %) are displayed. At the strain level of 2.2 %, one strain localization emerges in the band 15, which shows much higher strain values than other bands. With the increasing load during the tensile test, more bands with strain localization present, as shown by the other two strain curves at the strain levels of 3 % and 6 %. Thus, this deformation stage can be characterized as a dynamic process with the strain localization phenomenon. It can therefore be named by the localized deformation regime.

Figure 20 exhibits the strain evolution trend in final deformation stage, in which three strain curves at different

Fig. 18 The strain evolution trend in regime I
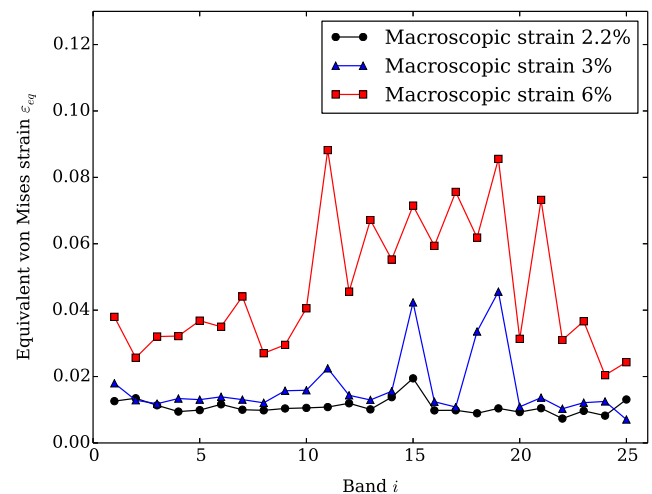
Fig. 19 The strain evolution trend in regime II

Fig. 20 The strain evolution trend in regime III

macroscopic strain levels (12 %, 14 %, 16 %) are illustrated. Apart from their difference in absolute strain levels, the three displayed strain curves demonstrate a very similar pattern. It indicates that the strain pattern (with respect to the band) tends to be stabilized in this stage. Hence, the final deformation stage is dominated by a stabilized deformation regime, whose intensity equally increases in bands with the loading.

The above analysis reveals that three deformation regimes can be determined from the evolution of strain fields. They are regime I - homogeneous deformation regime, regime II - localized deformation regime and regime III - stabilized deformation regime. The proposed band-based analysis approach shows its utility in describing the main features of the deformation regimes in a simple and straightforward manner. To the best of our knowledges, in the study of single crystal plasticity there is no publication that reports the classification and determination of the deformation regimes based on the strain heterogeneity evolution, though the importance of the deformation bands played in the work hardening process has long been noticed by the Japanese researchers [41, 42]. The new methodology proposed in this work is potential to be linked with the classical definition on the work hardening stages [10] in single crystal deformation.

Conclusion

An innovative DIC methodology has been developed in this work that is dedicated to characterize a heterogeneous deformation process in single crystals. This method was applied successfully to a pure nickel single crystal specimen deformed by multiple slip.

The developed DIC methodology can be summarized by the following steps: 1) Computation of the displacement fields using B-spline transformations; 2) Determination of the "domains" related to the slip bands from the obtained displacement fields; 3) Projection of the displacement data within the determined domains through analytic functions; 4) Resolving of the strain fields by differentiating the analytic functions for each band. A key parameter in this methodology is the selection of the grid spacing e in the B-spline transformation. To model the local deformation properly, the e value should be suitable, allowing both the preservation of local slip behaviors and avoidance of unexpected noises. The varied e values also provide a solution for resolving the displacement field "purely" related to the slip activation, and so as to determine the physical basis for the projection.

Some preliminary results of the strain field evolution obtained using the proposed method were presented. Based on the evolution of the deformation pattern during the tensile test, three deformation regimes can be determined. They are regime I -homogeneous deformation regime, regime II - localized deformation regime and regime III - stabilized deformation regime. Further analysis shows that the spatial and temporal features of the three deformation regimes are inherently associated with the slip activation, i.e., the emergence and development of slip bands on the crystal surface.

The developed DIC methodology provide a promising tool to study the mechanical behaviors of single crystals. It is prospected to be used for establishing further quantitative relationships between slip activity and deformation pattern evolution. And potentially, it provides a new angle to revisit the plastic deformation mechanism of single crystals and related phenomena, e.g., work hardening, from the point of view of strain heterogeneity.

References

1. Magid KR, Florando JN, Lassila DH, LeBlanc MM, Tamura N, Morris JW (2009) Mapping mesoscale heterogeneity in the plastic deformation of a copper single crystal. Phil Mag 89(1):77–107

2. Devincre B, Kubin LP, Lemarchand C, Madec R (2001) Mesoscopic simulations of plastic deformation. Mater Sci Eng A 309-310:211–219

3. Roters F, Eisenlohr P, Hantcherli L, Tjahjanto DD, Bieler TR, Raabe D (2010) Overview of constitutive laws, kinematics, homogenization and multiscale methods in crystal plasticity finite-element modeling: theory, experiments, applications. Acta Mater 58(4):1152–1211

4. Efstathiou C, Sehitoglu H, Lambros J (2010) Multiscale strain measurements of plastically deforming polycrystalline titanium Role of deformation heterogeneities. Int J Plast 26(1):93–106

5. Feaugas X (1999) On the origin of the tensile flow stress in the stainless steel AISI 316L at 300 k: back stress and effective stress. Acta Mater 47(13):3617–3632

6. Kramer DE, Savage MF, Levine LE (2005) AFM Observations of slip band development in al single crystals. Acta Mater 53(17):4655–4664

7. Feaugas X, Haddou H (2007) Effects of grain size on dislocation organization and internal stresses developed under tensile loading in fcc metals. Phil Mag 87(7):989–1018

8. Blewitt TH, Coltman RR, Redman JK (1955) Dislocations and mechanical properties of crystals. Wiley, New York

9. Mecking H, Kocks UF (1981) Kinetics of flow and strain-hardening. Acta Metall 48(3):1865–1875

10. Kocks UF, Mecking H (2003) Physics and phenomenology of strain hardening: the FCC case. Prog Mater Sci 48(3):171–273

11. Taylor GI, Elam CF (1923) Bakerian lecture. the distortion of an aluminium crystal during a tensile test. Proc Royal Soc London Ser A 102(719):643–667

12. Chin GY, Thurston RN, Nesbitt EA (1966) Finite plastic deformation due to crystallographic slip. Trans Metall Soc AIME 236:69–76

13. Basinski ZS, Basinski SJ (2004) Quantitative determination of secondary slip in copper single crystals deformed in tension. Phil Mag 84(3-5):213–251

14. Chu TC, Ranson WF, Sutton MA (1985) Applications of digital-image-correlation techniques to experimental mechanics. Exp Mech 25(3):232–244

15. Sutton MA, Orteu JJ, Schreier H (2009) Image correlation for shape, motion and deformation measurements: Basic Concepts, Theory and Applications. Springer, New York

16. Pan B (2011) Recent progress in digital image correlation. Exp Mech 51(7):1223–1235

17. Grédiac M, Hild F (2012) Full-field measurements and identification in solid mechanics. Wiley, New York

18. Kammers AD, Daly S (2013) Digital image correlation under scanning electron microscopy: Methodology and validation. Experimental Mechanics 53(9):1743–1761

19. Besnard G, Hild F, Roux S (2006) "Finite-element" displacement fields analysis from digital images: application to portevin-le châtelier bands. Exp Mech 46(6):789–803

20. El Bartali A, Aubin V, Degallaix S (2008) Fatigue damage analysis in a duplex stainless steel by digital image correlation technique. Fatigue Fract Eng Mater Struct 31(2):137–151

21. Bodelot L, Charkaluk E, Sabatier L, Dufrénoy P (2011) Experimental study of heterogeneities in strain and temperature fields at the microstructural level of polycrystalline metals through fully-coupled full-field measurements by digital image correlation and infrared thermography. Mech Mater 43(11):654–670

22. Li L, Latourte F, Muracciole JM, Sabatiera L, Wattrisse B (2015) Calorimetric analysis of coarse-grained polycrystalline aluminum by IRT and DIC. Quant InfraRed Thermography J 12(1):80–97

23. Zhao Z, Ramesh M, Raabe D, Cuitiño AM, Radovitzky R (2008) Investigation of three-dimensional aspects of grain-scale plastic surface deformation of an aluminum oligocrystal. Int J Plast 24(12):2278–2297

24. Saai A, Louche H, Tabourot L, Chang HJ (2010) Experimental and numerical study of the thermo-mechanical behavior of Al bi-crystal in tension using full field measurements and micromechanical modeling. Mech Mater 42(3):275–292

25. Florando JN, LeBlanc MM, Lassila DH (2007) Multiple slip in copper single crystals deformed in compression under uniaxial stress. Scr Mater 57(6):537–540

26. Efstathiou C, Sehitoglu H (2010) Strain hardening and heterogeneous deformation during twinning in hadfield steel. Acta Mater 58(5):1479–488

27. Charkaluk E, Seghir R, Bodelot L, Witz JF, Dufrénoy P (2015) Microplasticity in polycrystals A thermomechanical experimental perspective. Exp Mech 55(4):741–752

28. Wang XG, Witz JF, El Bartali A, Oudriss A, Jiang C (2015) Quantitative infrared thermography applied to subgrain scale and the effect of out-of-plane deformation. Infrared Phys Technol 71:432–438

29. Cheng P, Sutton MA, Schreier HW, McNeill SR (2002) Full-field speckle pattern image correlation with b-spline deformation function. Exp Mech 42(3):344–352

30. Hild F, Roux S (2012) Comparison of local and global approaches to digital image correlation. Exp Mech 52(9):1503–1519

31. Seghir R, Witz JF, Charkaluk E, Dufrénoy P (2012) Improvement of thermomechanical full-field analysis of metallic polycrystals using crystallographic data. Mech Ind 13(6):395–403

32. Lekbir C, Creus J, Sabot R, Feaugas X (2013) Influence of plastic strain on the hydrogen evolution reaction on nickel (100) single crystal surfaces to improve hydrogen embrittlement. Mater Sci Eng A 578:24–34

33. Klein S, Staring M, Murphy K, Viergever MA, Pluim JPW (2010) elastix: A toolbox for intensity-based medical image registration. IEEE Trans Med Imaging 29(1):196–205

34. http://elastix.isi.uu.nl/. [Online; accessed 10-Jan-2016]

35. Zitová B, Flusser J (2003) Image registration methods: a survey. Image Vis Comput 21(11):977–1000

36. Maintz JBA, Viergever MA (1998) A survey of medical image registration. Med Image Anal 2:1–36

37. Westerweel J (1997) Fundamentals of digital particle image velocimetry. Meas Sci Technol 8(12):1379–1392

38. Rueckert D, Sonoda LI, Hayes C, Hill DLG, Leach MO, Hawkes DJ (1999) Nonrigid registration using free-form deformations: Application to breast mr images. IEEE Trans Med Imaging 18:712–721

39. Unser M (1999) Splines: a perfect fit for signal and image processing. IEEE Signal Proc Mag 16(6):22–38

40. Hauser JJ, Jackson KA (1961) Effect of grip constraints on the tensile deformation of f.c.c. single crystals. Acta Metall 9(1):1–13

41. Higashida K, Takamura J, Narita N (1986) The formation of deformation bands in f.c.c. crystals. Mater Sci Eng 81:239–258

42. Takamura J (1987) Formation of deformation bands and work hardening of fcc crystals. Trans Jpn Inst Met 28(3):165–181